# SIMULATION OF AN ACOUSTICALLY INDUCED ELECTROMAGNETIC FIELD IN A BOREHOLE EMBEDDED IN A POROUS FORMATION

Hengshan Hu and Kexie Wang

Department of Physics
Jilin University
Changchun, 130023, China

Jingnong Wang

Jianghan Well Logging Institute
Qianjiang, Hubei, 433123, China

## ABSTRACT

When an acoustic point source located on the borehole axis emits an acoustic wave, an electric field, as well as an acoustic field, is generated in the porous formation around the borehole due to an electrokinetic effect. The coupled acoustic and electromagnetic wavefields were formulated by applying Pride's (1994) governing equations and boundary conditions at the borehole wall. Numerical examples show that two kinds of electric fields can be received on the borehole axis. The propagating electromagnetic wave arrives at different receivers almost simultaneously, and appears as the first wave packet in the full electric field waveform. Another kind of electric field accompanies the acoustic pressures, and consists of the same component waves as that of the acoustic waveforms.

On the borehole axis, the coupled electric field vector is in the axial direction on the borehole axis. A study of the ratio of the magnitude of electric field strength to the magnitude of pressure, or REP, shows that the compressional wave has the largest REP value, the Stoneley wave the next, and the shear wave the smallest. The peak value of the electric field strength at 1 kHz is about 100 times larger than that at 10 kHz, while the REP at 1 kHz is about five times larger than REP at 10 kHz. Off the borehole axis, the electric field has a radial and axial component, and one can also receive a circumferential magnetic field. When the interdependence between porosity, tortuosity and permeability is ignored, the REP increases rapidly with porosity, decreases with tortuosity, and changes little with permeability. The electric field strength decreases

with borehole fluid salinity and formation water salinity.

## INTRODUCTION

In sedimentary rocks, pore fluid usually contains conducting ions. While there are no net charges in the bulk porous medium, there is an electric double layer (EDL) at the matrix-fluid interface. One of the common models of EDL is the Stern-Guoy model (Pride and Morgan, 1991), consisting of a Stern layer and a diffuse layer. For sandstones, there are immovable anions in the Stern layer, which are balanced by a diffuse layer of movable cations in the fluid belt near the pore wall. When an acoustic wave propagates in a fluid saturated porous medium, the fluid and ions in the diffuse layer move relative to the solid matrix, causing a convection electric current and streaming potential. This phenomenon is called acoustoelectric (A-E) conversion. The reverse, electroosmosis phenomenon is called electroacousto (E-A) conversion, in which an electric field causes pore fluid flow. As these conversions are associated with electrical and mechanical properties of the pore fluid and rock frame, they may be potentially useful in hydrocarbon exploration.

Effort has been given to understanding the mechanism of this kind of electrokinetic effect. Zhu *et al.* (1994) observed an acoustically-induced electrical field in rock samples, and Zhu *et al.* (1999) measured acoustoelectric signals in scaled model wells in the laboratory. The center frequency of their transducer is higher than 10 kHz, although they call their observed phenomenon 'seismoelectric' conversion. Using the volume-averaging method, Pride (1994) derived from first principles the governing equations for acoustic and electromagnetic coupling in porous media. He assumed that the diffuse layer is thin when compared to pore size, and that the ions in the Stern layer do not contribute to conduction. Despite these and other assumptions in his derivation, Pride's theory seems an effective tool in explaining Zhu *et al.*'s (1994, 1999) experimental results. Pride's theory assumes the absence of a macroscopic static electric field before the arrival of acoustic disturbance. While we adopt this assumption in our work here, we point out that there is usually spontaneous potential (SP) around the borehole. The effect of SP on A-E conversion needs to be studied further. In this paper, we apply Pride's theory to formulate acoustic and electric fields in porous formation near a fluid-filled borehole, then simulate the wavefields in A-E logging. We see that the waveguide effect of the borehole is obvious if the frequency is in the order of kilohertz, which is the conventional acoustic logging frequency.

## FORMULATION

Coupled acoustic and electromagnetic fields in a homogeneous porous formation may be described by Pride's governing equations. Appendix A is a brief review of the Pride theory. Equation (A-1) shows coupling between mechanical motion and an electromagnetic field in the frequency domain. The dynamic permeability, $\kappa$, the formation conductivity, $\sigma$, and electrokinetic coupling coefficient, $L$, appearing in that equation are

important to the problem studied here. If $L$ were set to zero, Pride's equations separate to Maxwell equations for an electromagnetic field, and Biot's equations (Biot, 1962) for a mechanical field in porous media. $L$ is frequency-dependent, and can be determined by experiments in the low frequency range as was done by Li *et al.* (1995). The value of $L$ depends on many factors, such as pore geometry, pore fluid salinity, temperature, and chemical composition of the rock matrix. Measuring formation conductivity $\sigma$ has been one of the most effective methods in petroleum exploration, and many empirical relations between conductivity and other formation parameters have been set up. In our numerical simulation we will use the expressions for $\sigma$ and $L$ derived by Pride (1994) under a thin diffuse layer assumption. The concept of dynamic permeability was first proposed by Johnson *et al.* (1987), and is related to Darcy permeability $\kappa_0$, porosity $\phi$, tortuosity $\alpha_\infty$, characteristic pore size $\Lambda$, and frequency $\omega$. The expression for $L$, $\sigma$, and $\kappa$ are given in Appendix D.

In A-E logging the acoustic source is located in the borehole; there are neither acoustic nor electromagnetic sources outside the borehole. Here, we study the axisymmetric fields excited by a point pressure source on the borehole axis. Let us adopt the cylindrical coordinate system ($r$, $z$, $\theta$), with $z$ coinciding with the borehole axis, and the source being on the origin. In the porous formation, the P wave (compressional wave) and SV wave (shear wave whose motion is in the $r$-$z$ plane) are coupled with an electromagnetic TM (transverse magnetic) wave due to the electrokinetic effect. These waves are transformed at the borehole wall, and there will be electromagnetic waves in the borehole. In Appendix B, we derived expressions for the acoustic and electromagnetic fields from Pride's governing equations. In the borehole one can receive acoustic pressure $p$, radial and axial components of the electric field $E_r$ and $E_z$, and circumferential magnetic field $H_\theta$. Expressions for $p$, $E_r$, $E_z$, $H_\theta$ are given by equations (B-5) through (B-7), where coefficients $A_m$ and $B_e$ are determined by solving linear equation (C-2). As both the source and the media are assumed symmetrical about the borehole axis, the circumferential component of the electric field $E_\theta$, and radial and axial components of magnetic field $H_r$ and $H_z$ are zero.

## CONVERTED ELECTROMAGNETIC FIELD FOR A GIVEN FORMATION

Using the expressions in the frequency domain from Appendix B, we calculate the waveforms in the time domain using Fourier transform. For example, the acoustic pressure in the borehole is

$$p(t) = \frac{1}{2\pi} \int_{-\infty}^{+\infty} p(\omega) \cdot S_0(\omega) \cdot \exp(-i\omega t) d\omega, \tag{1}$$

Where $p(\omega)$ is given by equation (B-5), and $S_0(\omega)$ is the spectrum of the source pulse function $s_0(t)$. In the appendices, the symbol $p$ is used to represent pressure in the frequency domain. It is also used to represent pressure in the time domain in the text.

To model the pressure change of the acoustic source, a cosine pulse function $s_0(t)$, with a variable center frequency $f_0$, and a pulse width $T_c$ is used as follows:

$$s_0(t) = \begin{cases} \frac{1}{2}\left[1+\cos\frac{2\pi}{T_c}\left(t-\frac{T_c}{2}\right)\right]\cos 2\pi f_0\left(t-\frac{T_c}{2}\right), & 0 \le t \le T_c \\ 0, & t<0 \text{ or } >T_c \end{cases} . \qquad (2)$$

Figure 1 shows the waveform and spectrum of the source pulse with $f_0$ being 6 kHz and $T_c$ being 0.5 ms. In the following discussion, $f_0$ and $T_c$ will be given explicitly if different values are used. The expressions in Appendix B are established for an acoustic point source of a volume change type (Kurkjian and Chang, 1986). In our calculation the source is assumed to be of a pressure type as described by Tsang (1979), with the pressure amplitude being 1 kPa when measured 1 mm away from the source center. This is achieved by dividing expressions (B-6) and (B-7) for $\phi_m$, $E_r$, $E_z$ , $H_\theta$ by $\rho_0\omega^2$.

Next, we investigate the properties of the converted electromagnetic field for a given formation. The formation parameters are listed in Table 1, where $\rho_s$, $K_s$, and $\epsilon_s$are the density, the compressional modulus, and the permittivity of the solid phase of the formation, respectively, $\epsilon_0$ is the permittivity in the vacuum, and $K_b$ and $G_b$ are compressional and shear moduli of the drained frame. A quality factor of 100 is assumed for the borehole fluid compressional wave. For brevity sake, we will not explain the parameter unless it is different from that in Table 1. Table 2 lists calculated velocities and attenuation coefficients at frequencies of 2 kHz and 6 kHz. We see that the shear and fast compressional wave velocities change little with frequency, and that the electromagnetic and slow compressional waves are highly dispersive. The attenuation coefficient of the slow compressional wave is much higher than the other waves. The velocity of the formation electromagnetic wave, $V_{em}$, is much smaller than light speed in vacuum, but is two to three orders greater than the speed of the fast compressional wave, $V_f$.

First, we look at simulated waveforms when the receivers are 3 meters away from the acoustic source. In Figure 2, the dotted line is the acoustic pressure $p$, calculated using Pride's theory. For comparison, we also calculate an acoustic waveform using the Biot-Rausenbaum model (Rausenbaum, 1974; Wang and Dong, 1986; Schmitt *et al.*, 1988; Zhang *et al.*, 1995), and found it coincides with the dotted lines in Figure 2. As the acoustic signal is minimally decreased due to electrokinetic coupling, one can reason that the energy of the converted electromagnetic field in A-E logging is very weak.

In Figure 2, each component acoustic wave has a counterpart $E_z$ wave. We designate by REP the ratio of the peak value of each wave packet of $E_z$ to that of the counterpart wave packet of $p$. The REP is different for different component waves, as shown in Table 3. Although the electric component wave and the acoustic component wave accompany each other, they do not go in step. The reason for the phase shift needs to be studied further. In the full $E_z$ waveform, a wave arrives earlier than the compressional wave. In Figure 3, the distance to the source varies from 3 m to 5 m. Both the pressure waveform and the electric field waveform are scaled to their respective wave magnitudes at $z = 3$ m. We see that there is a type of wave that travels so fast that it arrives at five different

| medium parameters | | |
|---|---|---|
| Pore fluid and borehole fluid | Formation frame and pore geometry | Formation solid |
| density $\rho_f$, 1000 kg/m$^3$ | porosity $\phi$, 0.2 | density $\rho_s$, 2650 kg/m$^3$ |
| bulk modulus $K_f$, 2.25 GPa | permeability $k_0$, $1.0 \times 10^{-12}$ m$^2$ | bulk modulus $K_s$, 35.70 GPa |
| salinity $C_f$, 585 g/m$^3$ | tortuosity $\alpha_\infty$, 3 | permittivity $\epsilon_s$, 4 $\epsilon_0$ |
| viscosity $\eta_f$, 0.001 Pa · s | bulk modulus $K_b$, 14.39 GPa | |
| permittivity $\epsilon_f$, $80\epsilon_0$ | shear modulus $G_b$, 13.99 GPa | |
| acoustic source parameters, receiver position, and borehole radius | | |
| center frequency $f_0$, 6 kHz | pulse width $T_c$, 0.5 ms | borehole radius 0.1 m |
| axial distance to acoustic source $z$, 3 m | radial distance to acoustic source $r$, 0 m | |

Table 1: Default input parameters used in examples. $\epsilon_0$ is the vacuum permittivity. The characteristic pore size is assumed to be $\Lambda = \sqrt{8\kappa_0\alpha_\infty/\phi}$ in all examples. Parameters in this table are used implicitly unless stated explicitly.

| wave type | velocity symbol | velocity (m/s) | | attenuation (m$^{-1}$) | |
|---|---|---|---|---|---|
| | | at 2 kHz | at 6 kHz | at 2 kHz | at 6 kHz |
| fast compressional wave | $V_f$ | 3973.45 | 3978.24 | 0.00330 | 0.02048 |
| show compressional wave | $V_s$ | 428.45 | 595.45 | 23.75953 | 33.29026 |
| shear wave | $V_{sh}$ | 2457.36 | 2465.12 | 0.01376 | 0.08342 |
| formation TM wave | $V_{em}$ | 1,820,146.17 | 3,114,326.45 | 0.00708 | 0.01211 |
| bore fluid TM wave | $V_e$ | 470,156.49 | 804,505.74 | 0.02740 | 0.04687 |
| bore fluid compressional wave | $V_m$ | 1500.00 | 1500.00 | 0.04295 | 0.12578 |

Table 2: Calculated velocities and intrinsic attenuation coefficients.

| $f_0$ | field quantity | compressional wave | shear wave | Stoneley wave |
|---|---|---|---|---|
| 6 kHz | $p$ (Pa) | 0.0172 | 0.2784 | 0.5586 |
| | $E_z$ ($10^{-9}$ V/m) | 16.21 | 32.31 | 185.9 |
| | REP ($10^{-9}$ m$^2$/C) | 942.44 | 116.06 | 332.80 |
| 5 kHz | $p$ (Pa) | 0.0089 | 0.0729 | 0.8081 |
| | $E_z$ ($10^{-9}$ V/m) | 15.06 | 6.531 | 267.80 |
| | REP ($10^{-9}$ m$^2$/C) | 1688.91 | 89.38 | 331.39 |

Table 3: Magnitudes and REP of component waves at $z = 3$ m.

receivers at almost the same time. This is the same wave that travels at the formation electromagnetic velocity, $V_{em}$. When the borehole radius increases, this wave arrives later. If the borehole radius changes to 0.3 m from 0.1 m, the wave delays 0.13 ms, which is the time it takes for an acoustic wave in fluid to travel 0.2 meters. This wave is weak compared to the later wavetrain.

From the above analysis and Table 3, the following three characteristics of acoustoelectric conversion in the borehole are evident: (1) There are two kinds of converted electric fields—one propagating at $V_{em}$, which is approximately the conventional electromagnetic velocity in a water-saturated rock—and the other accompanying the acoustic waves, thus having an apparent velocity of the acoustic wave; (2) for the electromagnetic field that accompanies the acoustic waves, the compressional wave has the highest REP value, the shear wave has the smallest, and the Stoneley wave is somewhere in between; and (3) between each component acoustic wave and its counterpart electric field, there is a phase shift, which remains almost constant when the receiver moves from $z = 3$ m to $z = 5$ m.

Next, we examine the acoustoelectric conversion properties when there are changes in frequency. Figure 4 shows the pressure and electric field waveforms at $z = 3$ m when the source center frequency is 1 kHz and the time duration $T_c$ is 3 ms. Compared to the Stoneley wave, all other component waves are too small to be seen. This is consistent with borehole wave excitation analysis (Cheng and Toksöz, 1981), i.e., the lower the frequency, the stronger the excitation amplitude of the Stoneley wave. In Figure 4, the maximum amplitude of the electric field is 8.77 $\mu$V/m, which is much larger than that at 6 kHz. When the source center frequency increases to 10 kHz, the shear, pseudo-Rayleigh, and Stoneley waves are stacked together (see Figure 5). The compressional wave and its converted electrical field are obvious. In the full $E_z$ waveform, the relative amplitude of the electromagnetic wave traveling at $V_{em}$ is larger than that at lower frequencies. This is due to an increase of frequency in the ratio of the displacement current to the conduction current. Table 4 lists the magnitudes of the pressure, the electric field strength and the REP values at frequencies of 1, 5, 6, and 10 kHz. At lower frequencies the converted electric field is stronger and easier to receive. Two factors contribute to a larger $E_z$ of the Stoneley wave speed at a lower frequency: (1) a stronger Stoneley wave at a lower source frequency; and (2) an increasing coupling

| $f_0$ (kHz) | $T_c$ (ms) | p (Pa) | $E_z$ ($10^{-9}$ V/m) | REP ($10^{-9}$ m$^2$/C) | $E_z$ ($10^{-9}$ V/m) |
|---|---|---|---|---|---|
| 1 | 3.0 | 16.54 | 8766.00 | 529.99 | 151.20 |
| 5 | 0.8 | 0.8081 | 267.80 | 331.39 | 17.09 |
| 6 | 0.5 | 0.5586 | 185.90 | 332.80 | 16.74 |
| 10 | 0.4 | 1.0510 | 89.83 | 85.47 | 14.02 |
| 10 | 0.25 | 0.7233 | 83.02 | 114.78 | 12.59 |

Table 4: Magnitudes and REP of component waves when frequency changes.

coefficient $L$ with decreasing frequency. On the other hand, at a higher frequency, one can utilize component waves other than the Stoneley wave, especially the compressional wave that has the largest REP value. Additionally, at a higher frequency, one can utilize the propagating electromagnetic wave.

Finally, we study the acoustic field and electromagnetic field when receiver position changes. Figure 6 shows pressure and electric fields at $z = 0$. The direct pressure field is purposely excluded in calculating the pressure at the origin. The maximum reflected pressure amplitude is 17.1 Pa. The maximum converted electric field amplitude is 4.817 $\mu$V, which is 25.91 times larger than that at $z = 3$ m. Because a smaller source receiver distance causes the converted electric field strength to be larger, it is necessary to place the receiver nearer to the source when the signal to noise ratio is the main concern.

Looking at the case where the receiver is placed off the borehole axis, there will be a nonzero radial electric field, an axial electric field, and a circumferential magnetic field when $r \neq 0$. Figure 7 shows $E_z$, $E_r$, and $H_\theta$ at $r = 0.05$ m and $z = 3$ m. We notice that $E_r$ and $H_\theta$ are almost in phase, while there is a phase shift about a quarter of a period between them and $E_z$. We also notice that in the full $E_z$ and $H_\theta$ waveforms, the *head waves* that travel at the speed of $V_{em}$, are seen clearly, but are barely visible in the full $E_r$ full waveform.

## INFLUENCE OF FORMATION PARAMETERS ON ACOUSTOELECTRIC CONVERSION

In this section, we investigate the acoustic pressure and the converted electromagnetic field when formation parameters change. These parameters include porosity $\phi$, permeability $\kappa_0$, tortuosity $\alpha_\infty$ and pore fluid salinity $C$. We assume the solid phase parameters $K_s$, $\rho_s$, and $\epsilon_s$ are unchanged.

### Porosity

When $\phi$ changes, the drained-frame moduli $K_b$ and $G$ also change. By analyzing a large experimental database, Vernik (1998) proposed empirical velocity-porosity relations. From his empirical relations for pure sandstones, we deduced $K_b$ and $G$ for a given

| porosity | Fields with fast compressional velocity | | | Fields with Stoneley wave velocity | | | TM head wave |
|---|---|---|---|---|---|---|---|
| $\phi$ % | $p$ Pa | $E_z$ $10^{-9}$V/m | REP $10^{-9}$m$^2$/C | $p$ Pa | $E_z$ $10^{-9}$V/m | REP $10^{-9}$m$^2$/C | $E_z$ $10^{-9}$V/m |
| 10 | 0.0097 | 13.16 | 1356.70 | 1.4820 | 164.7 | 111.13 | 15.27 |
| 20 | 0.0172 | 16.21 | 942.44 | 0.5586 | 185.9 | 332.80 | 16.74 |
| 25 | 0.0287 | 27.90 | 970.77 | 0.4239 | 180.9 | 426.75 | 15.92 |
| 32 | 0.1128 | 71.17 | 630.94 | 0.2512 | 172.2 | 685.51 | 12.97 |
| See Table 1 for all other input parameters except the drained frame modulus | | | | | | | |

Table 5: Magnitudes and REP of component waves when porosity changes.

porosity. For porosities of 0.1, 0.2, 0.25, and 0.32, $K_b$ equals 22.627, 14.394, 12.093, and 5.891 GPa, and $G$ equals 22.225, 13.992, 10.828, and 4.63 GPa. The sandstone of 0.32 porosity is unconsolidated, and the other three sandstones are consolidated. The compressional and shear velocities are 3670 m/s and 2205 m/s, respectively, when $\phi$ is 0.25. When $\phi$ increases to 0.32, the shear velocity is 1480 m/s (which is less than the borehole fluid velocity). We assume that all input parameters besides the less important parameter $\Lambda$ do not change with porosity. The pore geometry relation $\Lambda = \sqrt{8\kappa_0\alpha_\infty/\phi}$ is used in the calculation, which is approximately valid for most sedimentary rocks (Johnson *et al.*, 1987). Figure 8a shows the waveforms of the pressure and the axial electric field in a formation of porosity 0.25; Figure 8b corresponds to a formation of porosity 0.32. Table 5 shows maximum magnitudes of $p$ and $E_z$ and the REP values for compressional and Stoneley waves. The amplitude of the Stoneley wave decreases when porosity increases, while the accompanying electric field changes very little. Thus, the REP value of the Stoneley wave increases with porosity. On the other hand, both the compressional wave and its accompanying electric field increase when porosity increases, and the REP value decreases with porosity.

## Permeability and Tortuosity

The formation permeability is related to many other parameters, such as porosity, clay content, tortuosity and pore size. Figure 9 shows $p$ and $E_z$ when $\kappa_0 = 1 \times 10^{-14}$ m$^2$. Comparing with Figure 2 where $\kappa_0 = 1 \times 10^{-12}$ m$^2$, we see that the amplitudes of the acoustic Stoneley wave and its converted electric field are sensitive to permeability. But REP changes so little with $\kappa_0$ that we see no advantage of A-E logging over conventional acoustic logging for permeability measurement. However, such a conclusion is obtained under an unrealistic assumption. In practical situations an increase in permeability usually accompanies an increase in porosity or a decrease in tortuosity. From Tables 5 and 6, one can see that REP increases with $(\phi/\alpha_\infty)$. Thus, we argue that REP increases with permeability if an increase in $(\phi/\alpha_\infty)$ accompanies an increase in $\kappa_0$. Noting that $(\phi/\alpha_\infty)$ is the reverse of the formation factor for pure sandstones, one can deduce that

| Permeability | P wave and converted $E_z$ | | | Stoneley wave and converted $E_z$ | | | TM wave |
|---|---|---|---|---|---|---|---|
| $\kappa_0$ $10^{-15}\mathrm{m}^2$ | $p$ Pa | $E_z$ $10^{-9}\mathrm{V/m}$ | REP $10^{-9}\mathrm{m}^2/\mathrm{C}$ | $p$ Pa | $E_z$ $10^{-9}\mathrm{V/m}$ | REP $10^{-9}\mathrm{m}^2/\mathrm{C}$ | $E_z$ $10^{-9}\mathrm{V/m}$ |
| 10 | 0.0135 | 20.73 | 1540.12 | 4.1580 | 1287.0 | 309.52 | 21.71 |
| 1000 | 0.0172 | 16.21 | 942.44 | 0.5586 | 185.9 | 332.80 | 16.74 |

Table 6: Magnitudes and REP of component waves when permeability changes.

| tortuosity | P wave and converted $E_z$ | | | Stoneley wave and converted $E_z$ | | | TM wave |
|---|---|---|---|---|---|---|---|
| $\alpha_\infty$ | $p$ | REP | $p$ | $E_z$ | REP | $E_z$ | |
| 3 | 0.0172 | 16.21 | 942.44 | 0.5586 | 185.9 | 332.80 | 16.74 |
| 5 | 0.0161 | 8.76 | 544.10 | 0.7373 | 125.4 | 170.08 | 14.44 |
| $p$: Pa; $E_z$ : $10^{-9}\mathrm{V/m}$; $E_z/p$ : $10^{-9}\mathrm{m}^2/\mathrm{C}$. | | | | | | | |

Table 7: Magnitudes and REP of component waves when tortuosity changes.

the REP value decreases with the formation factor. The relation between REP and permeability cannot be obtained quantitatively until a large database is set up for the relations between $\kappa_0$ and other parameters through experiments.

Furthermore, permeability decreases sharply when clay exists in the formation pores. The existence of clay means an increase of anions on the matrix surfaces, or cation exchange capacity (CEC), leading to a larger zeta potential. On the other hand, the existence of clay also increases the tortuosity of the pore channel. We cannot estimate the effect of clay content on REP. Experiments done by Li *et al.* (1995) show no obvious relation between CEC and the coupling coefficient $L_0$. The rock samples they use are limited, thus more experiments need to be performed on this aspect.

Table 7 shows the REP, the maximum magnitudes of pressure waveform, and the maximum magnitudes of the converted electric field waveform for $\alpha_\infty = a3$ and $\alpha_\infty = 5$. All other input parameters remain unchanged except $\Lambda$. We see that a formation with a larger tortuosity has a smaller REP value. While the accompanying electric field strength becomes much smaller, the amplitude of the electromagnetic head wave decreases slightly.

## Salinity

In the above examples, both the formation brine and borehole mud are assumed to have the same salinity of $C = 0.01$ mol/L. In a practical downhole environment, the borehole mud salinity may be higher or lower than that of the formation, giving rise to spontaneous potential. In our calculation, we ignore the effect of SP on acoustoelectric conversion. We also ignore possible small changes in acoustic velocity due to change in salinity. Table 8 shows the magnitudes of converted electric field strength under four different combinations of the borehole and formation salinity. Figure 10 shows full electric waveforms, where the dotted line, the fine solid line, and the thick solid line

| Salinity (mol/L) | | | $E_z$: V/m | | | |
|---|---|---|---|---|---|---|
| No. | bore fluid | formation | P wave | SV wave | Stoneley wave | TM wave |
| 1 | 0.01 | 0.01 | 16.210 | 32.310 | 185.9 | 16.74 |
| 2 | 0.01 | 0.1 | 2.543 | 6.631 | 38.48 | 0.623 |
| 3 | 0.1 | 0.01 | 1.952 | 3.579 | 20.64 | 9.708 |
| 4 | 0.1 | 0.1 | 0.663 | 1.322 | 7.61 | 0.685 |

Table 8: Magnitudes and REP of component waves when brine salinity changes.

correspond to salinity No. 2, No. 3, and No. 4 (in Table 8), respectively. The acoustic responses are not shown because they are almost the same as in Figure 2. For a given salinity of the borehole fluid, the amplitude of the converted electric field decreases when formation salinity increases. The amplitude of the converted electric field also decreases when borehole fluid salinity increases and formation water salinity is fixed. Salinity affects acoustoelectric conversion in two ways: First, an increase in formation water salinity makes the zeta potential smaller, and the surplus ions in the diffuse layer fewer, so the acoustoelectric coupling is weaker. Second, a change in either the formation water salinity or the borehole mud salinity makes the medium conductivity contrast different; thus, the reflection and refraction at the boundary behave differently.

## DISCUSSION AND CONCLUSIONS

Coupled acoustic and electromagnetic fields around a borehole were formulated by applying Pride's governing equations and boundary conditions. Acoustoelectric well logs were simulated. When a transducer emits an acoustic wave in a borehole, two kinds of electromagnetic fields, as well as acoustic pressure, can be received. One kind of electric field accompanies the acoustic wave. The other kind of wave travels with conventional electromagnetic wave speed, and arrives at different receivers at almost the same time.

The strength of the converted electric and magnetic fields depends not only on the coupling coefficient, but also on the borehole waveguide effect. We studied the factors affecting the REP value. These factors included source frequency, receiver position, porosity, permeability, and fluid salinity in and out of the borehole. At proper frequency and receiver positions, there are distinct compressional, shear, and Stoneley waves in the full acoustic waveform. For each of these component waves, there is an accompanying electric field. However, the REP value is different for different component waves. The compressional wave has the largest REP value, the Stoneley wave the next largest, and the shear and pseudo-Rayleigh wave group the smallest. The converted electric field at 1 kHz frequency is about 100 times as strong as that at 10 kHz, and REP increases by five. Two factors contribute to the increase in the magnitude of the converted field. First, the coupling coefficient is larger at a lower frequency. The more important factor is that a much larger Stoneley wave is excited at a lower frequency. Off the borehole axis there is a magnetic field as well as an electric field. REP increases when porosity

increases. If all the other parameters do not change when permeability changes, there is little change in REP, therefore, A-E logging has no advantage over conventional acoustic logging. However, in practical situations, either an increase in porosity or a decrease in tortuosity usually accompanies an increase in permeability. If these factors are taken into consideration, the REP value increases with permeability.

We note that the expression for the electrokinetic coupling coefficient (Eq. D-2) and the expression for the formation conductivity (Eq. D-3) are an integral part of Pride's theory. One of the many parameters that must be known in using these expressions is the zeta potential. It may vary with temperature and the chemical property of the formation matrix, as well as brine salinity. As the zeta potential is difficult to define in rocks, measuring DC or the low frequency electrokinetic coupling coefficient is more straightforward. More experiments must be done to understand the mechanism of electrokinetic coupling in rocks before we can discuss possible applications of acoustoelectric well logging.

## ACKNOWLEDGMENTS

The first author benefited from discussions with Professor Nafi Toksöz and Dr. Zhenya Zhu at the Massachusetts Institute of Technology. This work was supported by the China National Natural Science Foundation, Grant No. 49674226.

## REFERENCES

Biot, M.A., 1962, Mechanics of deformation and acoustic propagation in porous media, *J. Appl. Phys., 33,* 1482–1483.

Cheng, C.H. and Toksöz, M.N., 1981,Elastic wave propagation in a fluid-filled borehole and synthetic acoustic log, *Geophysics, 47,* 1042–1053.

Hu, H. and Wang, K., 1999, Axisymmetric coupled acoustic and electromagnetic waves around a borehole, Part 1: Formulation, *Well Logging Technology, 22* (in Chinese), 427–432.

Johnson, D.L., Koplik, J., and Dashen, R., 1987, Theory of dynamic permeability and tortuosity in fluid-saturated porous media, *J. Fluid Mech., 176,* 379–402.

Kurkjian, A.L. and Chang, S.K., 1986, Acoustic multipole sources in fluid-filled boreholes, *Geophysics, 51,* 148–163.

Li, S.X., Pengra, D.B., and Wang, P.Z., 1995, Onsagers reciprocal relation and the hydraulic permeability of porous media, *Phys. Rev. E, 51,* 5748–5751.

Pride, S.R., 1994, Governing equations for the coupled electromagnetics and acoustics of porous media, *Phys. Rev. B., 50,* 15678–15696.

Pride, S.R. and Haartsen, M.W., 1996, Electroseismic wave properties, *J. Acoust. Soc. Am., 100,* 1301–1315.

Pride, S.R. and Morgan F.D., 1991, Electrokinetic dissipation induced by seismic waves, *Geophys ics, 56,* 914–925.

Rosenbaum, J.H., 1974, Synthetic microseismograms: logging in porous formations, *Geophysics, 39,* 14–32.

Schmitt, D.P., Bouchon, M., and Bonnet, G., 1988, Full-wave synthetic acoustic logs in radially semiinfinite saturated porous media, *Geophysics, 53,* 807–823.

Tsang, L., Rader, D., 1979, Numerical evaluation of transient acoustic waveforms due to a point source in a fluid-filled borehole, *Geophysics, 44,* 1706–1720.

Vernik, L., 1998, Acoustic velocity and porosity systematics in siliciclastics, *The Log Analyst,* 27–35.

Wang, K. and Dong, Q., 1986, Theoretical Analysis and calculation of sound field in an oil well surrounded by a permeable formation, *Acta Petrolei Sinica, 7,* 59–69.

Zhang, B., Wang, K., and Dong, Q., 1995, Theory of acoustic multipole logging and analysis of wave components and calculation of full waveforms for two-phase medium formation, *Acta Geophysica Sinica, 38,* 178–192.

Zhang, S.K., Liu, H.L., and Johnson, D.L., 1988, Low frequency tube waves in permeable rocks, *Geophysics, 53,* 519–527.

Zhu, Z., Cheng, C.H., and Toksöz, M.N, 1994, Electrokinetic conversion in a fluid-saturated porous rock sample, *Expanded Abstracts, 64th Ann. Inernat. Mtg., Soc. Expl. Geophys.*, 425–427.

Zhu, Z., Haartsen, W.H., and Toksöz, M.N., 1999, Experimental studies of electrokinetic conversions in fluid-saturated borehole models, *Geophysics, 64,* 1349–1356.

# Appendix A. PRIDE THEORY FOR A FLUID-FILLED POROUS FORMATION

Pride (1994) derived from first principles the governing equations for coupled acoustic and electromagnetic waves in a porous medium. Besides the assumptions adopted in Biots theory (1962), Pride made two assumptions for coupling between mechanical motion and electric fields: (1) The ion distribution in the radial direction of the pore is of the Gouy-Stern type, with the diffuse layer thickness being much smaller than the pore diameter; and (2) ions in the Stern layer do not contribute to conduction. For harmonic fields with time dependence of $\exp(-i\omega t)$, coupling between mechanical motion and electric field are expressed as follows.

$$\begin{aligned} \mathbf{J} &= \sigma\mathbf{E} + L(-\nabla p + \omega^2\rho_f\mathbf{u}) \\ -i\omega\mathbf{w} &= L\mathbf{E} + (-\nabla p + \omega^2\rho_f\mathbf{u})\kappa/\eta \end{aligned} \tag{A-1}$$

where $\mathbf{u}$ is the solid frame displacement, $\mathbf{w}$ is the volume average relative filtration displacement, $\mathbf{E}$ is the electric field, $\rho_f$ and $\eta$ are density and viscosity of the pore fluid, respectively, and $\kappa$, $\sigma$, and $L$ are the dynamic permeability, conductivity, and electrokinetic coupling coefficient of the formation, respectively. Expressions for calculating $\kappa$, $\sigma$, and $L$ are given in Appendix D. Equations (A-1a) and (A-1b) are generalizations of Ohms law and Darcys law, respectively. The filtration velocity $-i\omega\mathbf{w}$ is related to $\mathbf{E}$ as well as pore fluid pressure gradient $\nabla p$ and inertial force $\omega^2\rho_f\mathbf{u}$. Osmotic motion, as well as the electric field, contributes to electric current density $\mathbf{J}$.

In the frequency domain, $\mathbf{u}$, $\mathbf{w}$, and $\mathbf{E}$ obey the following set of equations (Pride and Haartsen, 1996).

$$(H-G)\nabla\nabla\cdot\mathbf{u} + G\nabla^2\mathbf{u} + \omega^2\rho\mathbf{u} + C\nabla\nabla\cdot\mathbf{w} + \omega^2\rho_f\mathbf{w} = 0$$

$$C\nabla\nabla\cdot\mathbf{u} + \omega^2\rho_f\mathbf{u} + M\nabla\nabla\cdot\mathbf{w} + \omega^2\tilde{\rho}\mathbf{w} - i\omega\tilde{\rho}L\mathbf{E} = 0$$

$$\nabla\nabla\cdot\mathbf{E} - \nabla^2\mathbf{E} - \omega^2\mu\tilde{\epsilon}\mathbf{E} + i\omega^3\mu\tilde{\rho}L\mathbf{w} = 0 \tag{A-2}$$

where $\epsilon$ is the permittivity of the formation, $\tilde{\epsilon} = \epsilon + i\sigma/\omega - \tilde{\rho}L^2$ is effective electrical permittivity of the formation, $\rho$ is density of the formation, $\tilde{\rho} = i\eta/(\omega\cdot\kappa)$ is the effective density for relative flow, $G$ is the shear modulus of the formation, and $H$, $C$, and $M$ are porous medium moduli. In terms of porosity $\phi$, bulk moduli of the solid grain $K_s$ and the fluid $K_f$, and densities of the grain $\rho_s$ and fluid $\rho_f$. The formation parameters $\rho$ $H$, $l$, $C$, and $M$ are defined by

$$\begin{aligned} \rho &= (1-\phi)\rho_s + \phi\rho_f, \\ H &= K_b + 4G/3 + (K_s - K_b)^2/(D - K_b), \\ C &= K_s(K_s - K_b)/(D - K_b), \\ M &= K_s^2/(D - K_b), \end{aligned}$$

where $D = K_s[1 + \phi(K_s/K_f - 1)]$.

Once $\mathbf{u}$, $\mathbf{w}$, $\mathbf{E}$ are known, all other quantities can be determined. Specifically, the stress tensor $\mathbf{t}$ and pore fluid pressure $p$ can be determined by the constitutive equations, which are the same as those in Biot theory, i.e.,

$$\tau = (H - 2G)(\nabla \cdot \mathbf{u})\mathbf{I} + C(\nabla \cdot \mathbf{w})\mathbf{I} + G(\nabla \mathbf{u} + \nabla \mathbf{u}^T) \quad \text{(A-3)}$$

$$-p = C\nabla \cdot \mathbf{u} + M\nabla \cdot \mathbf{w} \quad \text{(A-4)}$$

and the magnetic field can be determined by Faradays law

$$\mathbf{B} = -i(\nabla \times \mathbf{E})/]\omega. \quad \text{(A-5)}$$

Finally, the constitutive equation for magnetic field,

$$\mathbf{H} = \mathbf{B}/\mu \quad \text{(A-6)}$$

where $\mu$ is the magnetic permeability of the formation, and is assumed to be equal to the vacuum magnetic permeability.

According to the derivation of Pride and Haartsen (1996), four types of waves can exist in an infinite uniform porous medium. Their slowness $s_f$, $s_s$, $s_{sh}$, and $s_{em}$ can be calculated as

$$2s_{f,s}^2 = \gamma \pm \sqrt{\gamma^2 - \frac{4\rho\tilde{\rho}}{MH - C^2}\left(\frac{\rho_t}{\rho} + \frac{\tilde{\rho}L^2}{\tilde{\epsilon}}\right)} \quad \text{(A-7)}$$

$$2s_{sh,em}^2 = \frac{\rho_t}{G} + \mu\tilde{\epsilon}\left(1 + \frac{\tilde{\rho}L^2}{\tilde{\epsilon}}\right) \pm \left\{\left[\frac{\rho_t}{G} - \mu\tilde{\epsilon}\left(1 + \frac{\tilde{\rho}L^2}{\tilde{\epsilon}}\right)\right]^2 - 4\mu\frac{\rho_f^2 L^2}{G}\right\}^{1/2} \quad \text{(A-8)}$$

where

$$\gamma = \frac{\rho M + \tilde{\rho}H(1 + \tilde{\rho}L^2/\tilde{\epsilon}) - 2\rho_f C}{HM - C^2},$$

$$\rho_t = \rho - \rho_f^2/\tilde{\rho},$$

when $L \to 0$, $s_f$, $s_s$, and $s_{sh}$ approach fast and slow compressional and shear slowness in a Biot medium, respectively, and $s_{em}$ approaches the electromagnetic slowness in the formation.

## Appendix B. THE ACOUSTIC AND ELECTROMAGNETIC FIELD EXPRESSIONS

Consider an axisymmetric medium system consisting of the borehole fluid and the formation. A point pressure source located at the origin will excite axisymmetric P-SV waves in the formation. The filtration displacement **w** and corresponding streaming current are also axisymmetric. So the electromagnetic wave is a wave of TM (transverse magnetic) type. As a result, an axisymmetric acoustic field is associated with an axisymmetric electric field. We adopt the cylindrical coordinate system $(r, z, \theta)$, and let $z$ be the axis of the borehole. According to Pride and Haartsen (1996), there are four different modes of waves in an infinite homogeneous fluid-saturated porous medium. Two of them are nonrotational waves. The other two are nondivergent waves. Similar to Zhang *et al.* (1988), we express **u**, **w**, **E** by potential functions as below.

$$\begin{aligned}
\mathbf{u} &= A_f \nabla\phi_f + A_s \nabla\phi_s + A_{sh} \nabla \times (\Gamma_{sh}\mathbf{i}_\theta) + A_{em} \nabla \times (\Gamma_{em}\mathbf{i}_\theta) \\
\mathbf{w} &= \alpha_f A_f \nabla\phi_f + \alpha_s A_s \nabla\phi_s + \alpha_{sh} A_{sh} \nabla \times (\Gamma_{sh}\mathbf{i}_\theta) + \alpha_{em} A_{em} \nabla \times (\Gamma_{sh}\mathbf{i}_\theta) \\
\mathbf{E} &= beta_f A_f \nabla\phi_f + \beta_s A_s \nabla\phi_s + \beta_{sh} A_{sh} \nabla \times (\Gamma_{sh}\mathbf{i}_\theta) + \beta_{em} A_{em} \nabla \times (\Gamma_{sh}\mathbf{i}_\theta)
\end{aligned} \tag{B-1}$$

where $\phi_f$ is associated with the fast compressional wave whose slowness is $s_f$, $\phi_s$ is associated with the slow compressional wave whose slowness is $s_s$; $\Gamma_{sh}$ is associated with the shear wave whose slowness is $s_{sh}$, and $\Gamma_{em}$ is associated with the electromagnetic wave whose slowness is $s_{em}$. The factors $\alpha_f$, $\alpha_s$, $\alpha_{sh}$, $\alpha_{em}$, $\beta_f$, $\beta_s$, $\beta_{sh}$, and $\beta_{em}$ are as below (Pride and Haartsen, 1996).

$$\begin{aligned}
\alpha_i &= -\tfrac{Hs_i^2-\rho}{Cs_i^2-\rho_f}, && i = f, s \\
\beta_i &= \tfrac{i\omega L\tilde{\rho}}{\tilde{\epsilon}} \left(\tfrac{Hs_i^2-\rho}{Cs_i^2-\rho_f}\right), && i = f, s \\
\alpha_i &= \tfrac{G}{\rho_f}\left(s_i^2 - \tfrac{\rho}{G}\right), && i = sh, em \\
\beta_i &= -i\omega\mu\tilde{\rho}L\tfrac{G}{\rho_f}\left(\tfrac{s_i^2-\rho/G}{s_i^2-\mu\tilde{\epsilon}}\right). && i = sh, em
\end{aligned} \tag{B-2}$$

When the coupling coefficient $L$ approaches zero, $\alpha_f$ and $\alpha_s$ are ratios of the filtration displacement to the solid frame displacement for fast and slow compressional waves, respectively, and $s_{sh}$ is the ratio of the filtration displacement to the solid frame displacement for shear wave.

In order for **u**, **w**, **E** expressed as in (B-1) to be solutions to equation (A-2), the scalar potential function $\phi_f$ must satisfy scalar Helmholtz equation with a wavenumber $l_f = \omega s_f$, and the vector potential function $(\Gamma_{sh}\mathbf{i}_\theta)$ must satisfy vector Helmholtz equation with a wavenumber $l_{sh} = \omega s_{sh}$. Similarly are $\phi_s$ and $(\Gamma_{em}\mathbf{i}_\theta)$. Outside the borehole $(r > a)$, the solutions are

$$\begin{aligned}
\phi_i &= K_0(\eta_i r)e^{ikz}, \quad \eta_i = \sqrt{k^2 - l_i^2} \quad i = f, s \\
\Gamma_j &= K_1(\eta_j r)e^{ikz}, \quad \eta_j = \sqrt{k^2 - l_j^2} \quad j = sh, em
\end{aligned} \tag{B-3}$$

where $k$ is the axial wavenumber, $\eta_i$ and $\eta_j$ are radial wavenumber, and where and hereafter $I_n$ and $K_n$ are modified Bessel functions of the $n$th order.

Substituting (B-3) into (B-1) one can get expressions for **u**, **w**, **E**. Using equations (A-3) through (A-6) one can obtain expressions for $\tau$, $p$, **H**. Here, we do not write explicitly the resultant expressions for **u**, **w**, **E**, **t**, $p$ and **H**, but readers can refer to Hu and Wang (1999). Thus, all field quantities in the porous formation are determined once coefficients $A_f$, $A_s$, $A_{sh}$, and $A_{em}$ are determined by boundary conditions.

The expressions for fields in the borehole are much simpler because the acoustic field and the electromagnetic field are not coupled. The pressure and displacement excited by a point source at the origin can be represented by a scalar potential $\phi_m$ as

$$\mathbf{u} = \nabla\phi_m. \tag{B-4}$$

$$p(\omega) = p = \rho_0\omega^2\phi_m, \tag{B-5}$$

where $\rho_0$ is borehole fluid density. Assuming the source is of a volume change type as described by Kurkjian and Chang (1986), the scalar potential is

$$\phi_m = \frac{1}{\pi}\int_{-\infty}^{\infty}[K_0(\eta_m r) + A_m I_0(\eta_m r)]\exp(ikz)dk \tag{B-6}$$

where $\eta_m = \sqrt{k^2 - l_m}$, $l_m$ is the acoustic wavenumber of the borehole fluid.

For A-E logging, there is no electric source in the borehole. The electric field must satisfy the Helmholtz equation $\nabla^2\mathbf{E}+l_e^2\mathbf{E} = 0$, where $l_e$ is the electromagnetic wavenumber in the borehole fluid. The electric field must also satisfy the nondivergence condition $\nabla \bullet \mathbf{E} = 0$. The solution is given by

$$\begin{aligned} E_r &= \int_{-\infty}^{\infty} B_e I_1(\eta_e r)\exp(ikz)dk \\ e_z &= \int_{-\infty}^{\infty} B_e \frac{\eta_e}{ik} I_0(\eta_e r)K_0(\eta_e r)\exp(ikz)dk \end{aligned}$$

From equations (A-5) and (A-6), one can obtain the magnetic field. The only nonzero component is

$$H_\theta = \frac{1}{\omega\mu}\int_{-\infty}^{\infty} B_e\left(k - \frac{\eta_e^2}{k}\right) I_1(\eta_e r)\exp(ikz)dk \tag{B-7}$$

The coefficients $A_m$ and $B_e$ can be determined by the boundary conditions in Appendix C. In equations (B-6) and (B-7) the time dependence is $\exp(-i\omega t)$.

## Appendix C. THE BOUNDARY CONDITIONS

To determine the coefficients in equations (B6), (B-7) and (B-1), the following conditions are applied:

$$\begin{aligned} u_{r0} &= u_{r1} + w_{r1}; \\ p_0 &= p_1; \\ -p_0 &= \tau_{rr1}; \\ 0 &= \tau_{rz1}; \\ E_{z0} &= E_{z1}; \\ H_{\theta 0} &= H_{01}. \end{aligned} \tag{C-1}$$

where quantities with subscript 0 are fields in the borehole, and quantities with subscript 1 are fields in the formation.

Using equations (B-4) through (B-7), one can get expressions for the left sides of the above boundary conditions: for the right sides, one can use equations (B-1), (B-3), and (A-3) through (A-6). The formation magnetic permeability of the borehole fluid can be assumed to be the same as that of the formation. The above six boundary conditions lead to the following linear equations.

$$\mathbf{MA} = \mathbf{B} \tag{C-2}$$

where

$$\mathbf{A} = \{A_m, B_e, A_f, A_s, A_{sh}, A_{em}\}^T, \tag{C-3}$$

$$\mathbf{B} = \{\eta_m K_1(\eta_m a)/\pi, -\omega^2 \rho_0 K_0(\eta_m a)/\pi, -\omega^2 \rho_0 K_0(\eta_m a)/\pi, 0, 0, 0\}^T, \tag{C-4}$$

and where the elements of M are

$$
\begin{aligned}
m_{41} &= m_{51} = m_{61} = m_{12} = m_{22} = m_{32} = m_{42} = m_{63} = m_{64} = m_{25} = m_{26} = 0 \\
m_{11} &= \eta_m I_1(\eta_m a)/\pi m_{21} = m_{31} = \rho_0 \omega^2 I_0(\eta_m a)/\pi \\
m_{13} &= \eta_f (1+\alpha_f) K_1(\eta_f a), \\
m_{14} &= \eta_s (1+\alpha_s) K_1(\eta_s a), \\
m_{15} &= ik(1+\alpha_{sh}) K_1(\eta_{sh} a), \\
m_{16} &= ik(1+\alpha_{em}) K_1(\eta_{em} a), \\
m_{23} &= -l_f^2 (C + M\alpha_f) K_0(\eta_f a), \\
m_{24} &= -l_s^2 (C + M\alpha_s f) K_0(\eta_s a), \\
m_{33} &= 2G\eta_f K_1(\eta_f a)/a + \lfloor (2G - H - C\alpha_f) l_f^2 + 2G\eta_f^2 \rfloor \cdot K_0(\eta_f a), \\
m_{34} &= 2G\eta_s K_1(\eta_s a)/a + \lfloor (2G - H - C\alpha_f) l_s^2 + 2G\eta_s^2 \rfloor \cdot K_0(\eta_s a), \\
m_{35} &= 2ikG[\eta_{sh} K_0(\eta_{sh} a) + K_1(\eta_{sh} a)/a], \\
m_{36} &= 2ikG[\eta_{em} K_0(\eta_{em} a) + K_1(\eta_{em} a)/a], \\
m_{43} &= -2ik\eta_f K_1(\eta_f a), \\
m_{44} &= -2ik\eta_s K_1(\eta_s a), \\
m_{45} &= (k^2 + \eta_{sh}^2) K_1(\eta_{sh} a), \\
m_{46} &= (k^2 + \eta_{em}^2) K_1(\eta_{em} a), \\
m_{52} &= \eta_e I_0(\eta_e a)/ik, \\
m_{53} &= ik\beta_f K_0(\eta_f a), \\
m_{54} &= ik\beta_s K_0(\eta_s a), \\
m_{55} &= -\beta_{sh}\eta_{sh} K_0(\eta_{sh} a), \\
m_{56} &= -\beta_{en}\eta_{em} K_0(\eta_{em} a), \\
m_{62} &= i(\eta_e^2/k - k) I_1(\eta_e a), \\
m_{65} &= \beta_{sh} l_{sh}^2 K_1(\eta_{sh} a), \\
m_{66} &= \beta_{em} l_{em}^2 K_1(\eta_{em} a).
\end{aligned}
\tag{C-5}
$$

## Appendix D. EXPRESSIONS FOR $\kappa$, $\sigma$, AND $L$

The dynamic permeability $\kappa$, conductivity $\sigma$, and coupling coefficient $L$ appearing in Eq. 1 are all frequency dependent. In calculation we use expressions derived by Pride (1994). These expressions are as follows.

$$\frac{\kappa(\omega)}{\kappa_0} = \left[\left[1 - i\frac{\omega}{\omega_c}\frac{4}{m}\right]^{\frac{1}{2}} - i\frac{\omega}{\omega_c}\right]^{-1} \tag{D-1}$$

$$\frac{L(\omega)}{L_0} = \left[1 - i\frac{\omega}{\omega_c}\frac{m}{4}\left(1 - 2\frac{\tilde{d}}{\Lambda}^2\right)\left(1 - i^{\frac{3}{2}}\frac{\tilde{d}}{\delta}\right)^2\right]^{-} \frac{1}{2} \tag{D-2}$$

$$\frac{\sigma(\omega)}{\sigma_0} = 1 + \frac{2}{\sigma_f \Lambda}[C_{em} + C_{os}(\omega)]. \tag{D-3}$$

where $\kappa_0$ is Darcy permeability, $m$ is a dimensionless parameter defined as $m = \phi\Lambda^2/\alpha_\infty\kappa_0$ and assumed to be 8 in calculation, $\alpha_\infty$ is tortuosity, $\Lambda$ is the characteristic pore size, $\omega_c = \phi\eta/\alpha_\infty\kappa_0\rho_f$ is the transition frequency from viscous flow to inertial flow, $\delta = \sqrt{\eta/\omega\rho_f}$ is the viscous skin depth, $\tilde{d}$ is less than or equal to Debye length $d$,

$$\tilde{d} \leq d = \sqrt{\epsilon_f k_B T/e^2 z^2 N}, \tag{D-4}$$

$\epsilon_f$ is fluid permittivity, $k_B$ is Boltzman constant, $T$ is absolute temperature, $e$ is the electrical charge, $z$ is ionic valence of the solution, $N$ is ion concentration, $N = 6.022 \times 10^{26} \times$ molarity, $L_0$ is the low frequency limit of the coupling coefficient,

$$L_0 = -\frac{\phi}{\alpha_\infty}\frac{\epsilon_f \varsigma}{\eta}\left[1 - a\alpha_\infty\frac{\tilde{d}}{\Lambda}\right], \tag{D-5}$$

where $\varsigma$ is the potential on the slipping plane. When the electrical double layer is very thin, i.e., $\tilde{d} \ll \Lambda$, one has the approximate expression

$$L_0 \approx -(\phi\epsilon_f/\alpha_\infty\eta)\varsigma. \tag{D-6}$$

Pride and Morgan (1991) got an expression for $\varsigma$ based on experiments with brine saturated quartz sand. When molarity is $C$ (mole/liter), the average $\varsigma$ is

$$\varsigma = 0.008 + 0.026\log_{10}(C). \tag{D-7}$$

Formation conductivity is defined as $\sigma_0 = \sigma_f\phi/\alpha_\infty$ for pure quartz sand. The formation water conductivity can be calculated by $\sigma_f = e^2z^2N(b_+ + b_-)$, where $b_\pm$ is ionic mobility.

$$C_{em} = 4de^2z^2Nb\left[\cos h\left(\frac{ez\varsigma}{2kT}\right) - 1\right], \tag{D-8}$$

$$C_{os}(\omega) = \frac{(\epsilon_f \varsigma)^2}{2d\eta} P_0 \left(1 - \frac{2i^{3/2}}{P_0}\frac{d}{\delta}\right)^{-1}, \tag{D-9}$$

where

$$P_0 = \frac{16kTd^2N}{\epsilon_f \varsigma^2}\left[\cos h\left(\frac{ez\varsigma}{2kT}\right) - 1\right]. \tag{D-10}$$

In our calculation, $T$ is assumed to be 298 K, $b_+ = b_- = 3 \times 10^{11}$ m/s/N, and $z = 1$.

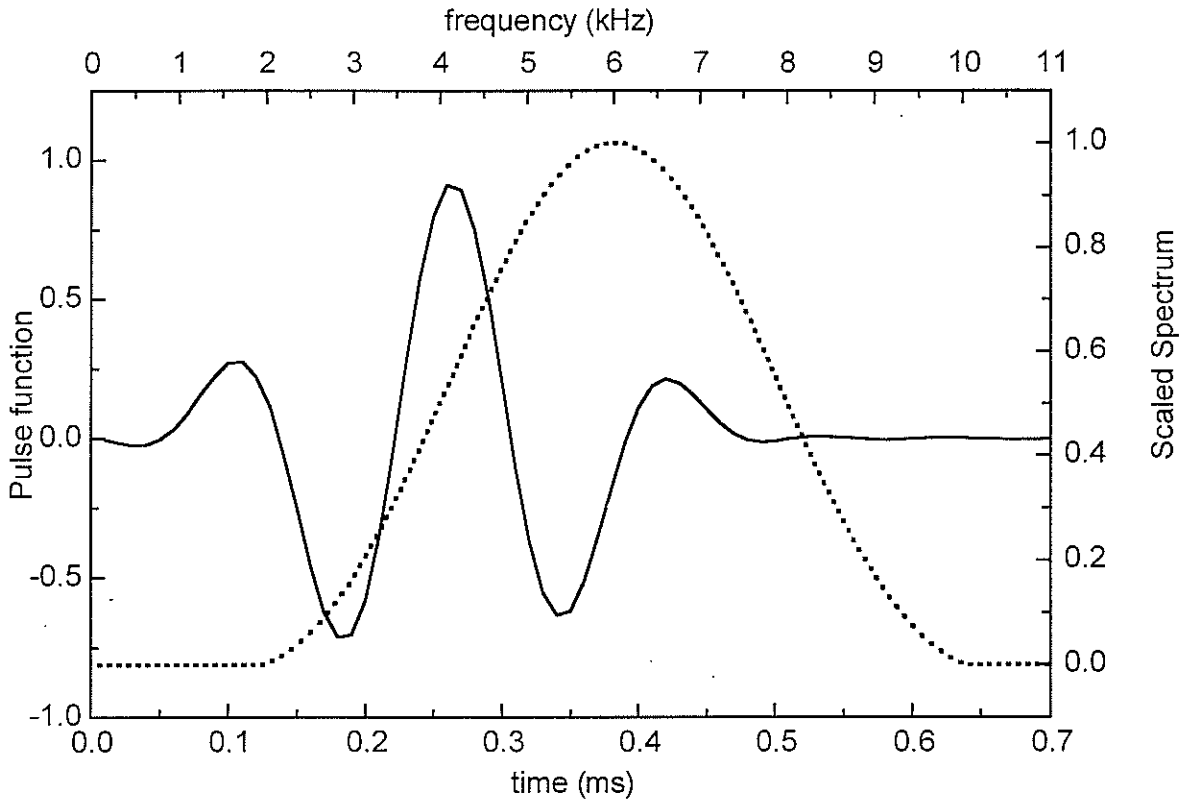


Figure 1: Pulse function of the acoustic source. The solid curve is the pulse function. The dotted line is the scaled spectrum.

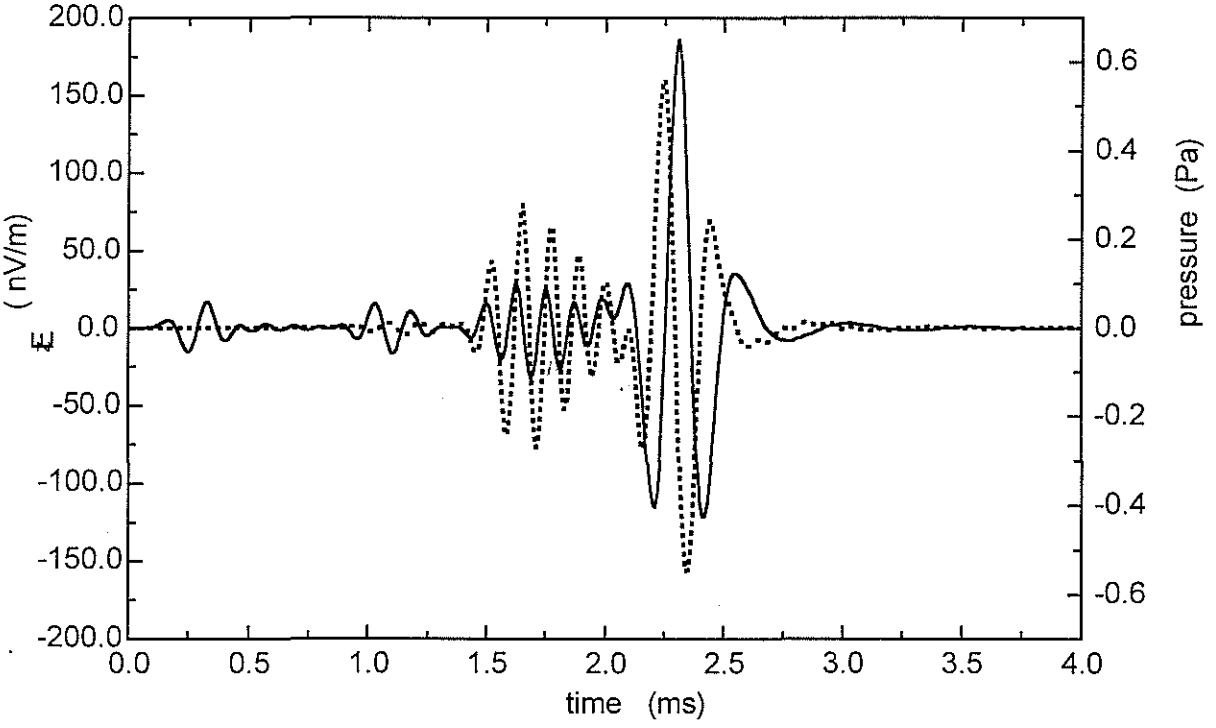


Figure 2: $p$ and $E_z$ on the borehole axis and at $z = 3$ m. The dotted line is $p$. The solid line is $E_z$. All input parameters are given in Table 1.

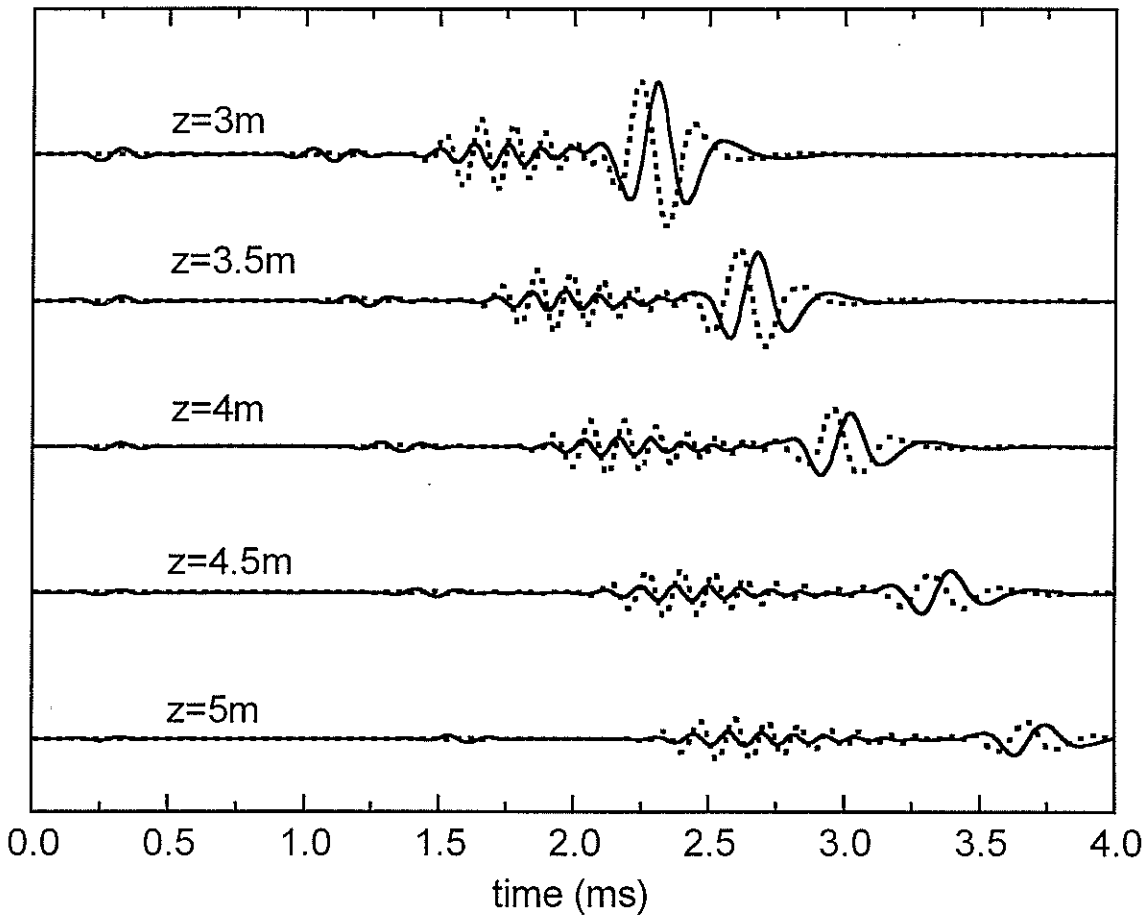


Figure 3: $p$ and $E_z$ when $z$ changes. $z$ increases from $z = 3$ m on the top to $z = 5$ m at the bottom. The dotted line is $p$. The solid line is $E_z$. The pressure waveforms are scaled relative to the maximum magnitude of pressure at $z = 3$ m. The electric field waveforms are scaled relative to the maximum magnitude of the electric field at $z = 3$ m.

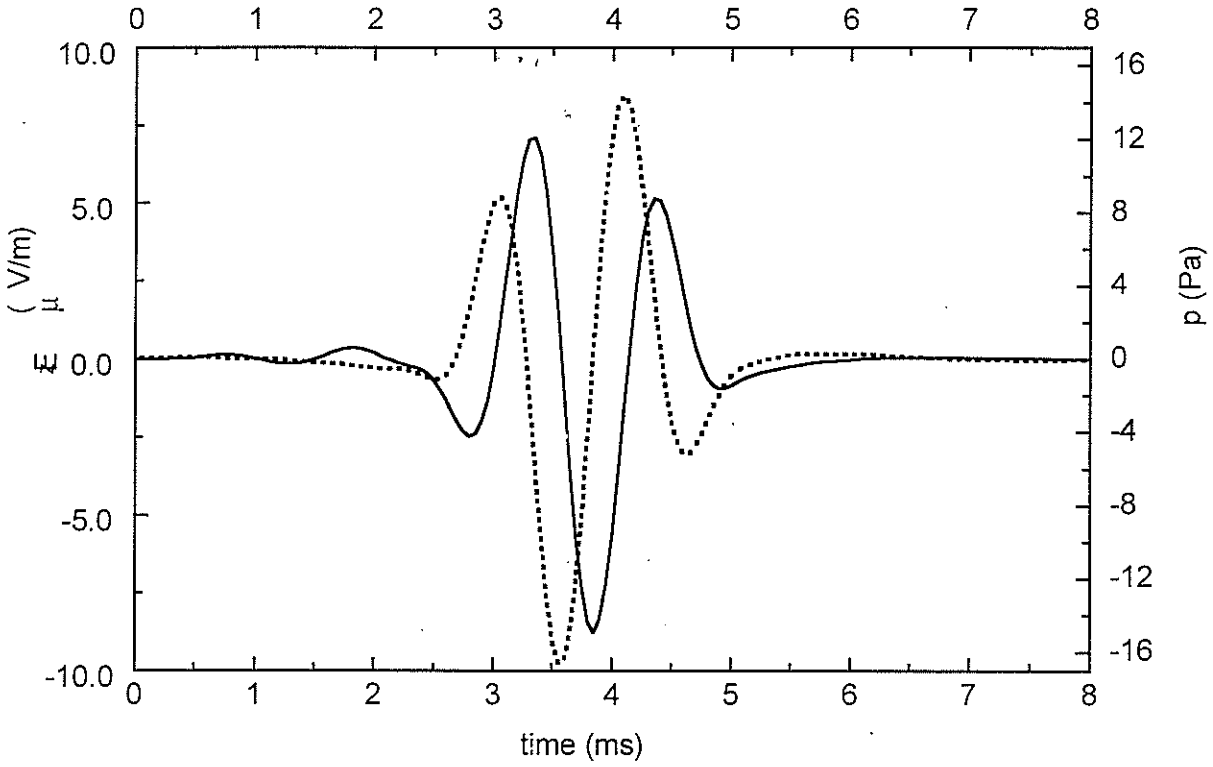


Figure 4: $p$ (dotted curve) and $E_z$ (solid curve) when the source frequency $f_0$ is 1 kHz and pulse duration $T_c$ is 3 ms. All the other input parameters are default parameters in Table 1.

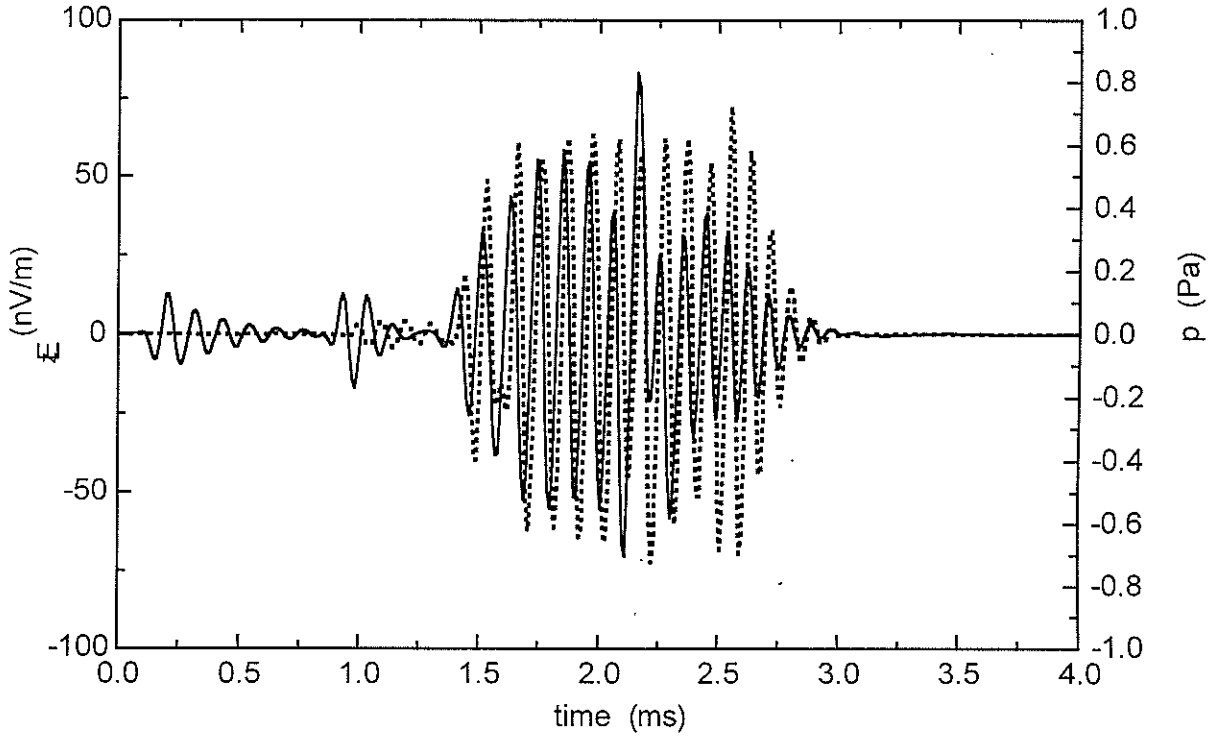


Figure 5: $p$ (dotted curve) and $E_z$ (solid curve) when the source frequency $f_0$ is 10 kHz and pulse duration $T_c$ is 0.25 ms. All the other input parameters are default parameters in Table 1.

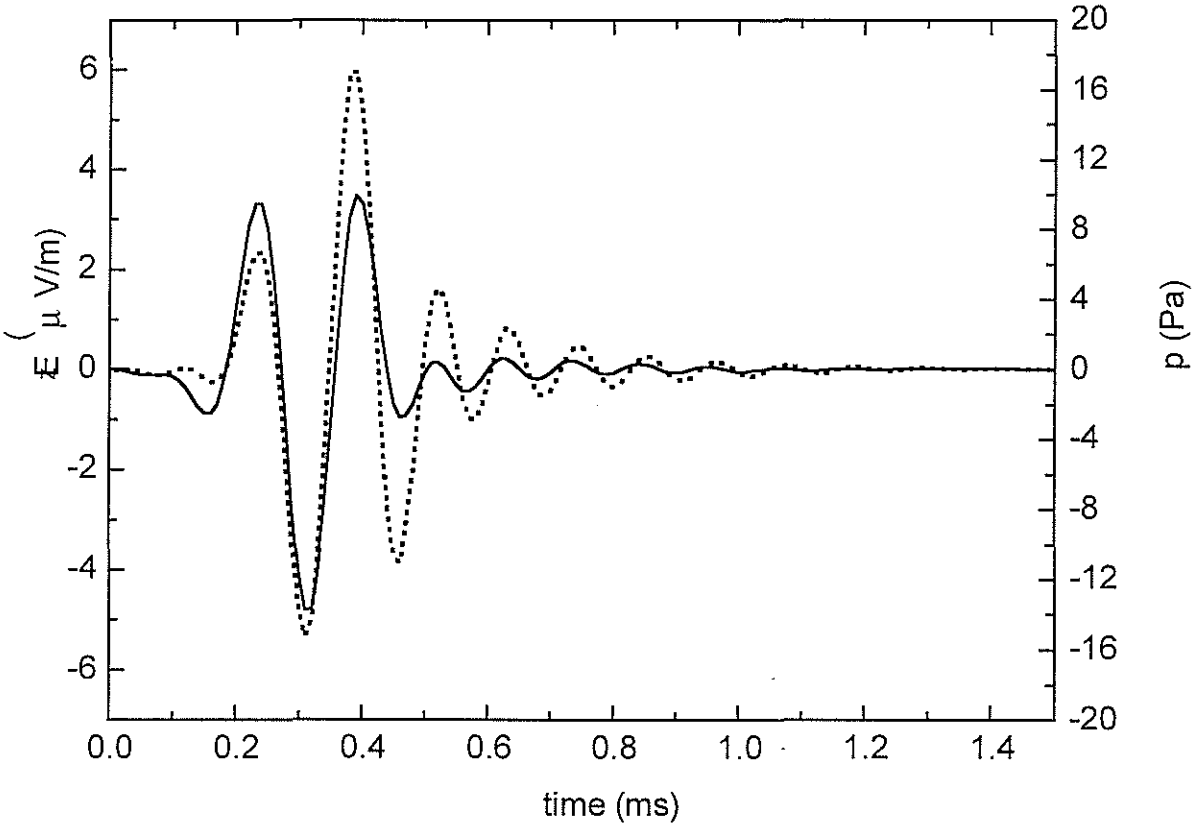


Figure 6: $p$ (dotted curve) and $E_z$ (solid line) at $z = 0$. All the other input parameters are default parameters in Table 1.

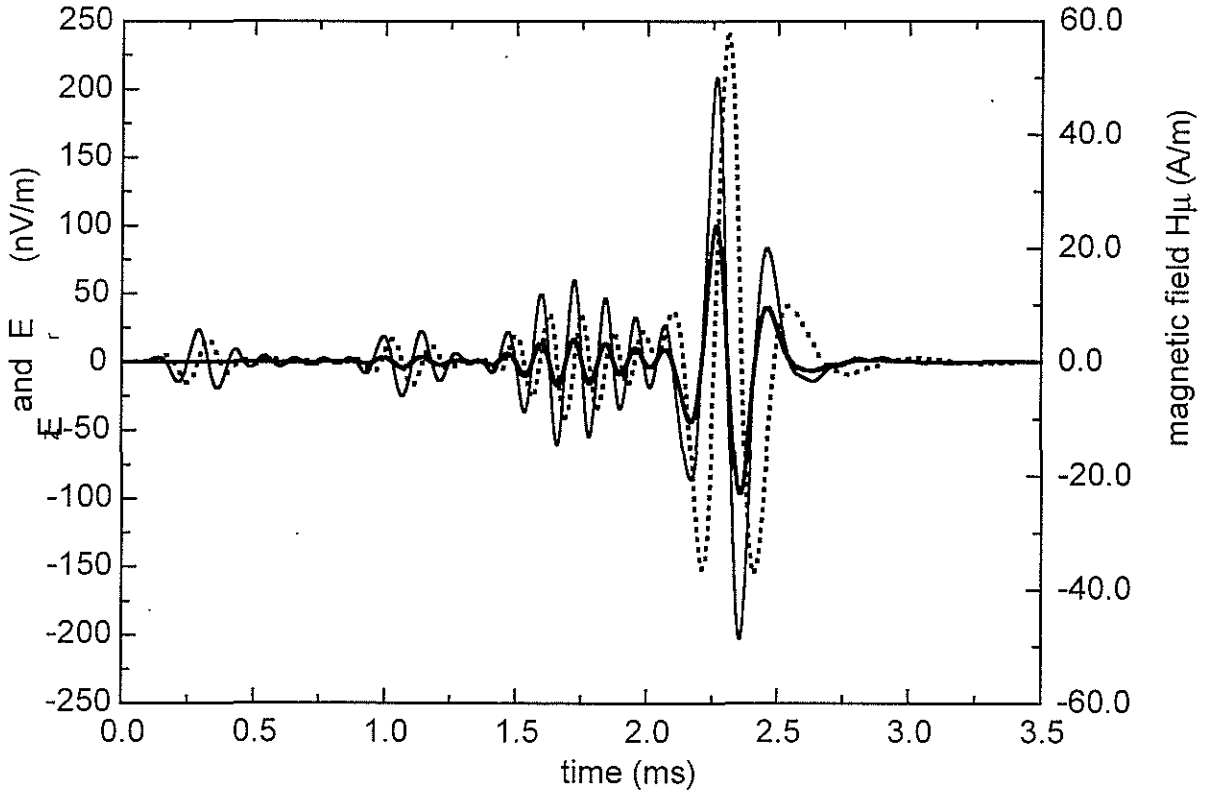


Figure 7: $E_z$ (dotted curve), $E_r$ (thick solid curve) and $H_\theta$ (fine solid curve) at $r = 0.05$ m and $z = 3$ m. All other input parameters are default parameters in Table 1.

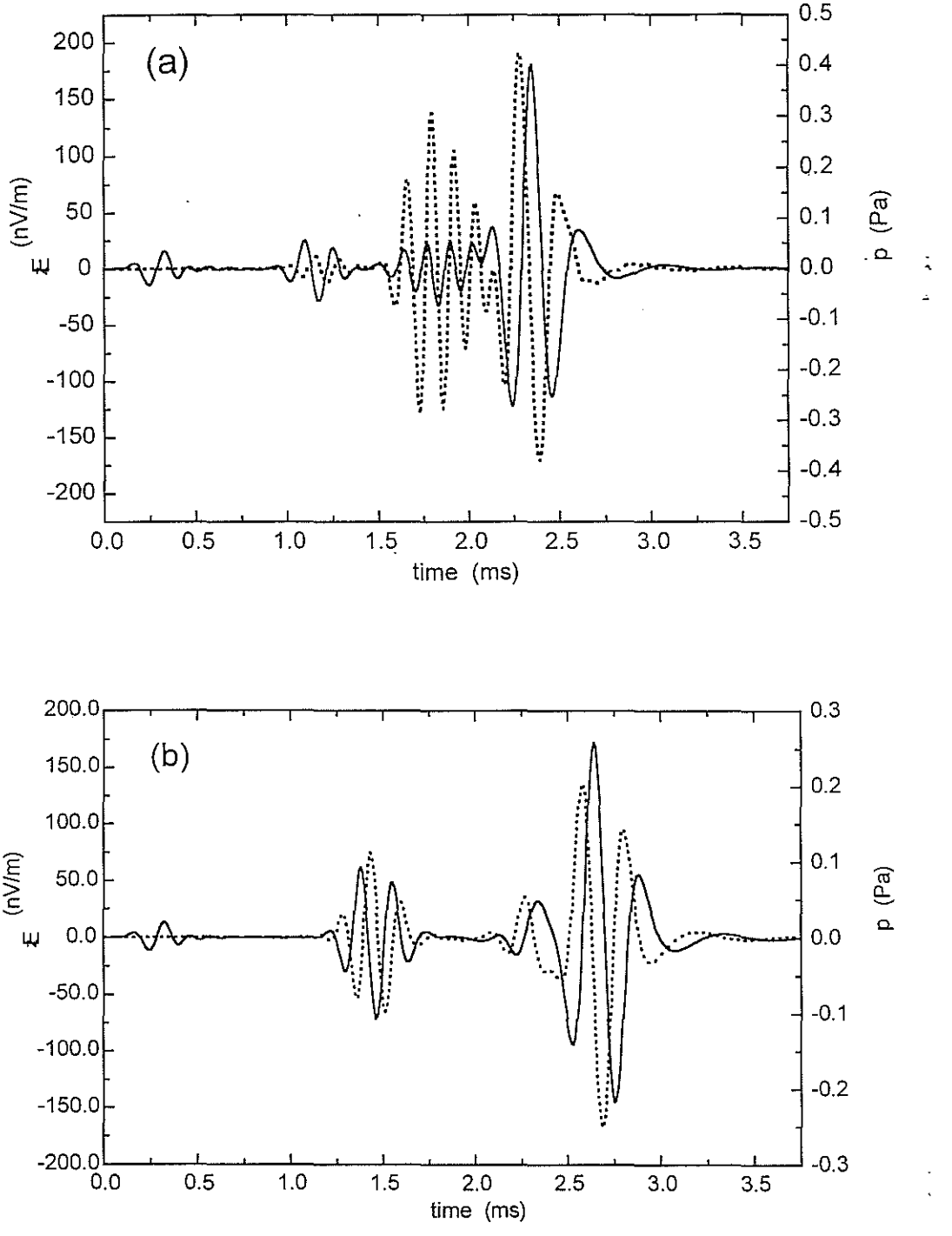


Figure 8: $p$ (dotted curve) and $E_z$ (solid line) for different porosities. (a) $\phi = 0.25$, (b) $\phi = 0.32$. All other input parameters are default parameters in Table 1.

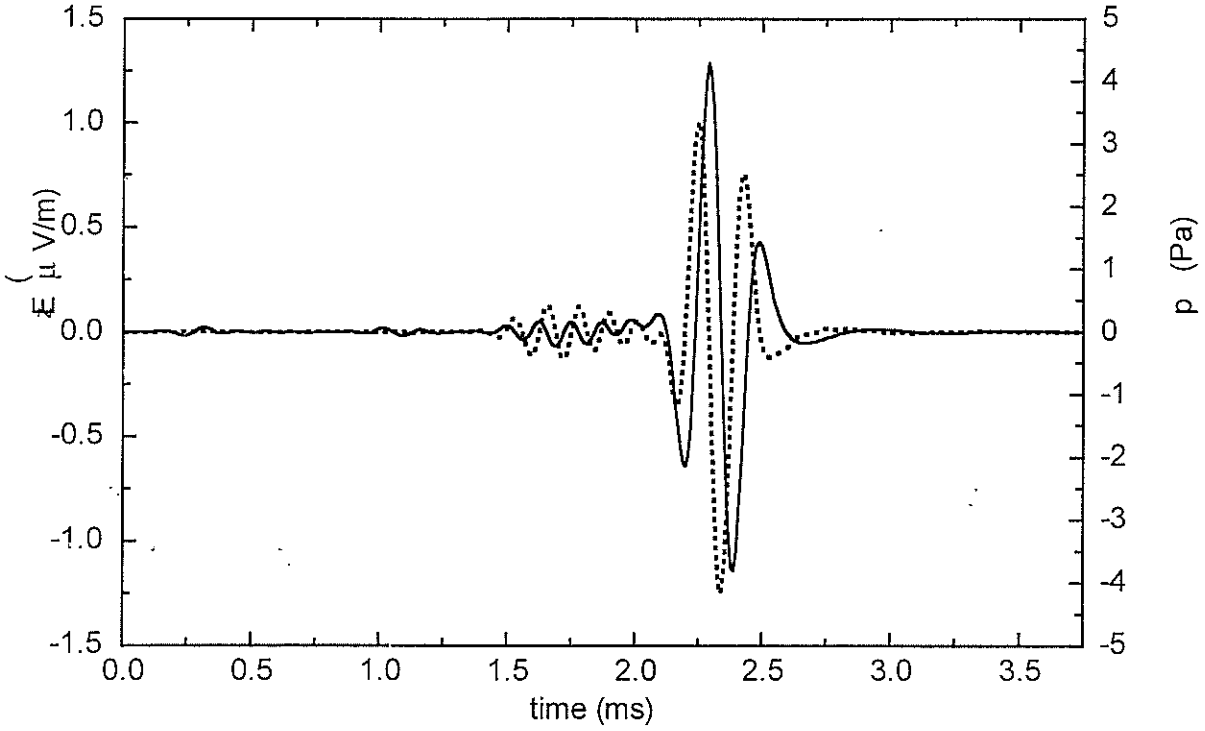


Figure 9: $p$ (dotted curve) and $E_z$ (solid line) when permeability is $\kappa_0 = 1 \times 10^{-14}$ m$^2$. All other input parameters are default parameters in Table 1.

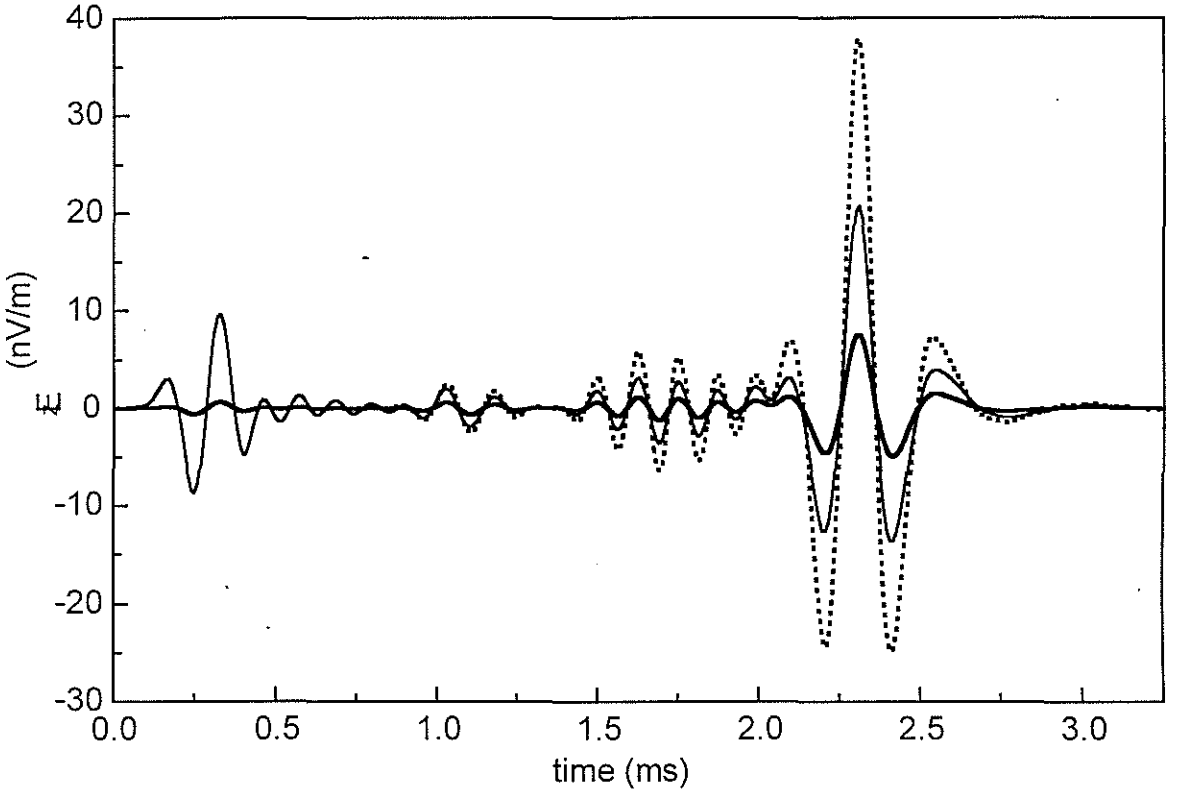


Figure 10: Axial electric field $E_x$ when salinity changes. The dotted line, the fine solid line, and the thick solid line correspond, respectively, to salinity combinations No. 2, No. 3, and No. 4 in Table 8. All other input parameters are default parameters in Table 1.